The Evolving Scholar Vol. 3, 2023 https://dx.doi.org/10.59490/65f89c8e269cb909bf53af3c

Bicycle and Motorcycle Dynamics 2023
Symposium on the Dynamics and Control of Single Track Vehicles
18 – 20 October 2023, Delft University of Technology, The Netherlands

Type of the Paper: Conference Paper

Development of a Hardware-in-the-Loop Test Bench for Validation of an Anti-lock Braking System on an E-Bike

N. Ramosaj[1], C. Fusco[1,2], E. Viennet[1,*]

[1]School of Engineering and Architecture of Fribourg, HES-SO University of Applied Sciences and Arts Western Switzerland; nicolas.ramosaj@hefr.ch; christia.fusco@hes-so.ch; emmanuel.viennet@hefr.ch ORCID 0009-0004-0922-2934
[2]Dipartimento di Ingegneria Meccanica e Aerospaziale, Politecnico di Torino, Italy
*Corresponding author

Name of Editor: Jason Moore
Submitted: 28/03/2024
Revised: 29/04/2024
Accepted: 02/05/2024
Published: 08/05/2024
Citation: Ramosaj, N., Fusco, C., & Viennet, E. (2023). Development of a Hardware-in-the-Loop Test Bench for Validation of an Anti-lock Braking System on an E-Bike. The Evolving Scholar – BMD 2023, 5th Edition.

Abstract

This article presents the development of a hardware-in-the-loop (HiL) test bench that can be used to validate an electric bicycle (e-bike) anti-lock braking system (ABS) in different test scenarios. The same e-bike can be used in a wide variety of loading conditions, such as with a child seat or panniers (mounted on the front or rear), and different types of tires. Therefore, validating the overall system—i.e., ABS and e-bike—over a wide range of parameters, such as the mass of the rider, load distribution, and tire characteristics, is challenging. The approach presented here involves interfacing a parameterizable virtual bicycle simulation model running on a real-time target machine with the physical ABS hardware under test. This article describes the derivation of an equation-based model that considers six degrees of freedom representing the in-plane longitudinal dynamics of an e-bike. The simulation model was experimentally validated against measurements made on an instrumented test bike. Tests carried out as part of this development show that the developed HiL test bench can be successfully interfaced with a commercially available ABS, enabling the overall behavior of the ABS and the e-bike to be tested and evaluated in a safe and reproducible way before testing begins on the track.

Keywords: bicycle, longitudinal dynamics, ABS, hardware-in-the-loop

ISSN: 2667-2812

 http://dx.doi.org/10.59490/65f89c8e269cb909bf53af3c

1 Introduction

Although electrically assisted bicycles (e-bikes) are becoming increasingly popular and can facilitate active commuting, this comes at the cost of safety because e-bikers have a higher risk of traffic accidents than traditional cyclists (Haufe et al., 2022). However, the availability of on-board electric power is enabling the emergence of active safety systems, such as an anti-lock braking system (ABS), which could help reduce the accident rate in the same way as has been observed in recent decades for cars and motorcycles (Maier, 2018). ABS has been widely used on cars since the 1970s and on motorcycles since the 1990s, but it was not until the 2010s that this technology was adapted to bicycles (Enisz et al., 2012; Maier et al., 2015; Corno et al., 2018).

ABS is a mechatronic device involving multi-domain expertise—encompassing electronics, mechanics, and software—and the results from these specific domains need to be integrated into an overall system to be validated. In the context of product development, as defined by the Association of German Engineers (VDI, 2004), the validation task consists of iteratively checking that the system characteristics match the requirements. Depending on which stakeholder is performing the validation and the level of the development cycle, different quantitative requirements may be defined. For example, a bike manufacturer looking to test an ABS purchased from a supplier on the e-bike it is developing could define the braking distance and lock-up duration as quantitative requirements. The braking distance can be defined as the distance covered between the start of braking and the bike coming to a complete stop. The lock-up duration is the total time during which the front wheel speed is zero while the bicycle is still moving forward.

In all cases, validation of an ABS implies being able to carry out braking tests with an integrated ABS on an e-bike. However, hard braking on two-wheelers, particularly when the front wheel locks, is a safety-critical maneuver. Therefore, it is particularly risky to carry out the initial validation of an ABS using road tests. Furthermore, in the case of road braking tests carried out by a human, it is difficult to achieve a sufficient level of reproducibility, particularly with regard to the application of braking force and the position or movement of the rider on the e-bike. In such a situation, a hardware-in-the-loop (HiL) test procedure offers an interesting way to validate an ABS in a safe and reproducible manner.

HiL testing is a well-established method for the development of mechatronic systems in the automotive industry, but its use is seldom reported for bicycle systems, with the notable exception of work carried out since 2015 at the Pforzheim University of Applied Sciences (Pfeiffer et al., 2020). HiL testing enables the design of a component (unit under test) to be validated without complete system hardware and relies on a real-time plant simulator that acts as a digital twin of the missing parts of the system. Setting up an HiL test bench for the validation of an ABS device involves capturing the longitudinal dynamic behavior of an electric bicycle in a virtual model run on a real-time plant simulator. The virtual bike model and the ABS hardware under test are then interfaced and interacted within a real-time closed loop. Figure 1a) presents the operating principle of an HiL test setup, and Figure 1b) shows the necessary components used in a real-time plant simulator.

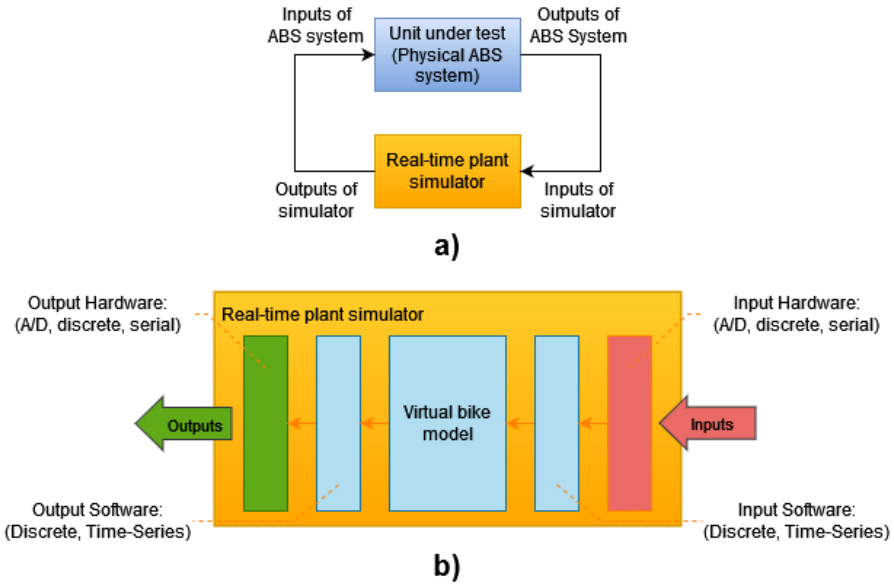

Figure 1. Operating principle of the hardware-in-the-loop test bench: a) unit under test and real-time plant simulator in closed loop; b) components of a real-time plant simulator (adapted from Gomez, 2001)

ISSN: 2667-2812

 http://dx.doi.org/10.59490/65f89c8e269cb909bf53af3c

Inputs to the real-time plant simulator may be provided by the software or graphical user interface (input software) or by the unit under test (input hardware) and must be sampled at the test bench operating frequency to be interpreted by the virtual model. The outputs of the virtual model must also be conditioned so that they can be interpreted by the hardware (output software). The numerical solvers generally available for real-time operation require that the model be formulated mathematically without algebraic loops. In addition, the level of modeling must be carefully chosen to avoid overloading the simulator processor.

This paper presents the development of a HiL test bench that can be used to validate the overall behavior of an ABS and a bicycle over the wide range of operating conditions that an e-bike may encounter. The test bench enables parameters such as rider mass, load distribution on the bike or tire grip characteristics on the road to be varied. The point of view adopted is that of an e-bike manufacturer wishing to validate the performance and robustness of an ABS whose technical implementation details are unknown, which is typically the case when the ABS is purchased from a supplier. The derivation of a simulation model based on six-degrees-of-freedom equations representing the in-plane longitudinal dynamics of an e-bike is presented in Section 2. The mobile test apparatus used on the e-bike for the validation of the model and the specific measurements carried out to experimentally characterize its front suspension and tires are presented in Section 3. The validation of the virtual bike model is presented in Section 4. Finally, Section 5 describes the developed HiL test bench and illustrates how it can be used to evaluate the braking performance of an ABS being tested on a crossover bike.

2 Equation-Based Modeling of In-Plane Dynamics

In this section, a mechanical model describing the longitudinal in-plane dynamics of a semi-rigid e-bike (front suspension only) is described. The model consists of four rigid bodies: the main body (bicycle frame + rider), the lower part of the fork, and the rear and front wheels, see Figure 2. It is assumed that the rider does not move with respect to the bicycle frame; therefore, their masses and inertias are lumped together at a common center of gravity (CoG) G. The inertia of the lower part of the fork is neglected, as it plays only a limited role in the overall dynamics of the system. To capture the in-plane motion of the frame, the travel of the front suspension, and the possible slip of the wheels, a model with six degrees of freedom was chosen. The generalized coordinates are grouped in a column vector denoted q and given by Equation (1):

$$q = [x_{\mathrm{G}}\ z_{\mathrm{G}}\ \theta_{\mathrm{G}}\ z_{\mathrm{FW}}\ \delta_{\mathrm{FW}}\ \delta_{\mathrm{RW}}]^{T}, \tag{1}$$

where x_{G} and z_{G} are the longitudinal and vertical displacement of the main body CoG, θ_{G} is the main body pitch angle, z_{FW} is the vertical displacement of the front wheel and δ_{RW} and δ_{FW} are the angular positions of the rear and front wheels relative to the frame.

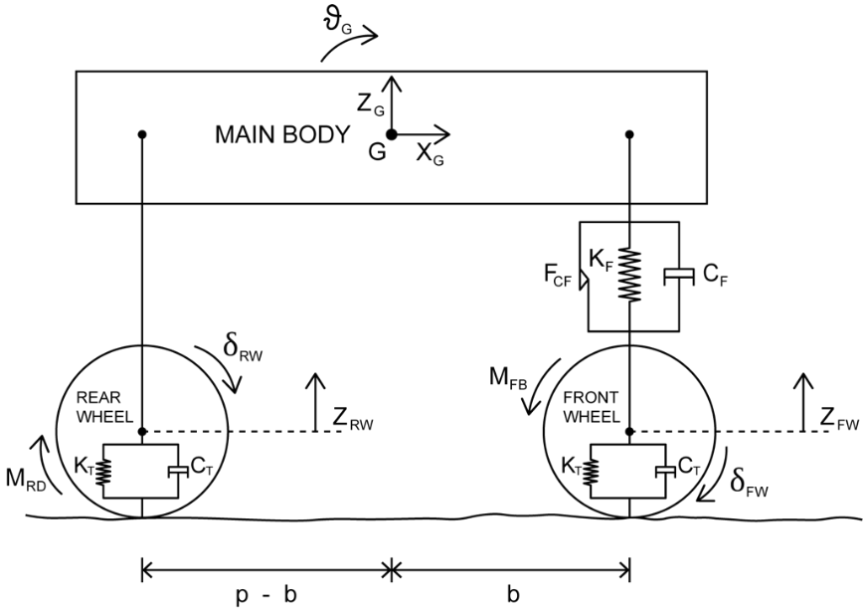

Figure 2. Bike model diagram

ISSN: 2667-2812

 http://dx.doi.org/10.59490/65f89c8e269cb909bf53af3c

Although a typical front suspension is characterized by a caster angle ϵ, we chose to reduce this to an equivalent vertical suspension to simplify the analysis, as described by Cossalter (2006). The equivalent stiffness k_{F} and damping c_{F} of the suspension can be expressed in terms of the actual stiffness k and damping c. In addition, a Coulomb friction force F_{CF} was considered in the suspension. A hyperbolic tangent function, associated with a gain k and the maximum friction force F_{C}, was used to relate the Coulomb friction force to the sign of the relative velocity v_{rel} of the suspension as shown in Equation (2):

$$k_{\mathrm{F}} = \frac{k}{\cos^2 \epsilon} \ , c_{\mathrm{F}} = \frac{c}{\cos^2 \epsilon} \ , F_{\mathrm{CF}} = -F_{\mathrm{C}} \cdot \tanh(k \cdot v_{\mathrm{rel}}). \tag{2}$$

The contact between the tire and the ground was modeled with a linear spring in parallel with a viscous friction. The notations used are summarized in Table 1.

Table 1. List of parameters

Name	Title	Unit
$main\ body$	"Frame + rider"	-
m_{b}	Mass of "main body"	kg
$m_{\mathrm{FW}}, m_{\mathrm{RW}}$	Mass of the front and rear wheels	kg
I_{b}	Inertia of "main body"	kgm^2
I_{FW}, I_{RW}	Inertia of the front and rear wheels	kgm^2
p	Wheelbase	m
b	Horizontal length from the front wheel axis to the CoG	m
h	Height from the front wheel axis to the CoG at static equilibrium	m
R_{FW}, R_{RW}	Front and rear wheel radius at static equilibrium	m
x_{G}, z_{G}	Displacement of *G* along the *x*- and *z*-axes	m
θ_{G}	Pitch angle	rad
z_{FW}	Displacement of the front wheel along the *z*-axis	m
δ_{FW}, δ_{RW}	Angular position of the front and rear wheels	rad
k_{F}	Stiffness of the equivalent vertical front suspension	N/m
c_{F}	Damping of the equivalent vertical front suspension	Ns/m
F_{CF}	Coulomb friction in equivalent vertical suspension	N
k	Numerical gain for tanh function	m/Ns
k_{T}	Stiffness of the front and rear tires	N/m
c_{T}	Damping of the front and rear tires	Ns/m
M_{FB}	Brake torque on the front wheel	Nm
M_{RD}	Driving torque on the rear wheel	Nm

Note. Moments of inertia are expressed about each component's center of gravity.

For a six-degrees-of-freedom problem with generalized coordinates q_j and generalized velocities $\dot{q}_j$, it is possible to formulate the Lagragian $L = T - V$, where T is the kinetic energy and V is the potential energy. The Lagrange equation is given in Equation (3):

$$\frac{d}{dt}\left(\frac{\partial L}{\partial \dot{q}_j}\right) - \left(\frac{\partial L}{\partial q_j}\right) = Q_j, \tag{3}$$

where Q_j denotes the nonconservative generalized forces, with the conservative forces being considered in the potential energy V.

ISSN: 2667-2812

 http://dx.doi.org/10.59490/65f89c8e269cb909bf53af3c

The generalized coordinates were measured from the static equilibrium position. Therefore, gravity is canceled by the initial spring forces and can be omitted from the potential energy. With a small angle approximation, the potential energy of the system can be expressed in Equation (4):

$$V = \frac{1}{2} \cdot k_{\mathrm{F}} \cdot (z_{\mathrm{G}} - \theta_{\mathrm{G}} \cdot b - z_{\mathrm{FW}})^2 + \frac{1}{2} \cdot k_{\mathrm{T}} \cdot z_{\mathrm{FW}}^2 + \frac{1}{2} \cdot k_{\mathrm{T}} \cdot \left(z_{\mathrm{G}} + \theta_{\mathrm{G}} \cdot (p - b)\right)^2. \tag{4}$$

The kinetic energy is given in Equation (5):

$$T = \frac{1}{2} \cdot m_{\mathrm{tot}} \cdot \dot{x}_{\mathrm{G}}^2 + \frac{1}{2} \cdot (m_{\mathrm{b}} + m_{\mathrm{RW}}) \cdot \dot{z}_{\mathrm{G}}^2 + \frac{1}{2} \cdot I_{\mathrm{tot}} \cdot \dot{\theta}_{\mathrm{G}}^2 + \frac{1}{2} \cdot I_{\mathrm{RW}} \cdot \dot{\delta}_{\mathrm{RW}}^2 + \frac{1}{2} \cdot m_{\mathrm{FW}} \cdot \dot{z}_{\mathrm{FW}}^2 + \frac{1}{2} \cdot I_{\mathrm{FW}} \cdot \dot{\delta}_{\mathrm{FW}}^2. \tag{5}$$

where m_{tot} and I_{tot} denote the total mass and inertia of the whole system, as expressed in Equation (6), with the approximation that the CoG of the whole system is identical to the CoG of the main body:

$$\begin{gathered} m_{\mathrm{tot}} = m_{\mathrm{b}} + m_{\mathrm{RW}} + m_{\mathrm{FW}} \\ I_{\mathrm{tot}} = I_{\mathrm{b}} + I_{\mathrm{RW}} + (h^2 + (p - b)^2) \cdot m_{\mathrm{RW}} + I_{\mathrm{FW}} + (h^2 + b^2) \cdot m_{\mathrm{FW}}. \end{gathered} \tag{6}$$

The generalized forces projected in the direction of each generalized coordinate are defined in Equation (7):

$$\begin{cases} Q_{x_{\mathrm{G}}} = -F_{x_{\mathrm{FW}}} - F_{x_{\mathrm{RW}}} \\ Q_{z_{\mathrm{G}}} = -\left((c_{\mathrm{F}} + c_{\mathrm{T}}) \cdot \dot{z}_{\mathrm{G}} + (c_{\mathrm{T}} \cdot (p - b) - c_{\mathrm{F}} \cdot b) \cdot \dot{\theta}_{\mathrm{G}} - c_{\mathrm{F}} \cdot \dot{z}_{\mathrm{FW}}\right) + F_{\mathrm{C}} \cdot tanh\left(k \cdot (\dot{z}_{\mathrm{FW}} + \dot{\theta}_{\mathrm{G}} \cdot b - \dot{z}_{\mathrm{G}})\right) \\ Q_{\theta_{\mathrm{G}}} = -((c_{\mathrm{T}} \cdot (p - b) - c_{\mathrm{F}} \cdot b) \cdot \dot{z}_{\mathrm{G}} + (c_{\mathrm{T}} \cdot (p - b)^2 + c_{\mathrm{F}} \cdot b^2) \cdot \dot{\theta}_{\mathrm{G}} - c_{\mathrm{F}} \cdot b \cdot \dot{z}_{\mathrm{FW}}) + \left(F_{x_{\mathrm{FW}}} + F_{x_{\mathrm{RW}}}\right) \cdot h \\ \qquad + F_{\mathrm{C}} \cdot tanh\left(k \cdot (\dot{z}_{\mathrm{G}} - \dot{\theta}_{\mathrm{G}} \cdot b - \dot{z}_{\mathrm{FW}})\right) \cdot b \\ Q_{z_{\mathrm{FW}}} = -\left(-c_{\mathrm{F}} \cdot \dot{z}_{\mathrm{G}} - c_{\mathrm{F}} \cdot b \cdot \dot{\theta}_{\mathrm{G}} + (c_{\mathrm{F}} + c_{\mathrm{T}}) \cdot \dot{z}_{\mathrm{FW}}\right) + F_{\mathrm{C}} \cdot tanh\left(k \cdot (\dot{z}_{\mathrm{G}} - \dot{\theta}_{\mathrm{G}} \cdot b - \dot{z}_{\mathrm{FW}})\right) \\ Q_{\delta_{\mathrm{FW}}} = F_{x_{\mathrm{FW}}} \cdot R_{\mathrm{FW}} - M_{\mathrm{FB}} \\ Q_{\delta_{\mathrm{RW}}} = M_{\mathrm{RD}} + F_{x_{\mathrm{RW}}} \cdot R_{\mathrm{RW}}. \end{cases} \tag{7}$$

By computing all the quantities and returning to Equation (3), the Lagrange equations can be expressed by the set of coupled ordinary differential equations in Equation (8):

$$\begin{cases} m_{\mathrm{tot}} \cdot \ddot{x}_{\mathrm{G}} = -F_{x_{\mathrm{RW}}} - F_{x_{\mathrm{FW}}} \\ \\ (m_{\mathrm{b}} + m_{\mathrm{RW}}) \cdot \ddot{z}_{\mathrm{G}} + (c_{\mathrm{F}} + c_{\mathrm{T}}) \cdot \dot{z}_{\mathrm{G}} - c_{\mathrm{F}} \cdot \dot{z}_{\mathrm{FW}} + (c_{\mathrm{T}} \cdot (p - b) - c_{\mathrm{F}} \cdot b) \cdot \dot{\theta}_{\mathrm{G}} \\ +(k_{\mathrm{F}} + k_{\mathrm{T}}) \cdot z_{\mathrm{G}} - k_{\mathrm{F}} \cdot z_{\mathrm{FW}} + (k_{\mathrm{T}} \cdot (p - b) - k_{\mathrm{F}} \cdot b) \cdot \theta_{\mathrm{G}} - F_{\mathrm{C}} \cdot tanh\left(k \cdot (\dot{z}_{\mathrm{FW}} + \dot{\theta}_{\mathrm{G}} \cdot b - \dot{z}_{\mathrm{G}})\right) = 0 \\ \\ \mathrm{I}_{\mathrm{tot}} \cdot \ddot{\theta}_{G} + (c_{\mathrm{F}} \cdot b^2 + c_{\mathrm{T}} \cdot (p - b)^2) \cdot \dot{\theta}_{\mathrm{G}} + (c_{\mathrm{T}} \cdot (p - b) - c_{\mathrm{F}} \cdot b) \cdot \dot{z}_{\mathrm{G}} + c_{\mathrm{F}} \cdot b \cdot \dot{z}_{\mathrm{FW}} \\ +(k_{\mathrm{F}} \cdot b^2 + k_{\mathrm{T}} \cdot (p - b)^2) \cdot \theta_{\mathrm{G}} + (k_{\mathrm{T}} \cdot (p - b) - k_{\mathrm{F}} \cdot b) \cdot z_{\mathrm{G}} + k_{\mathrm{F}} \cdot b \cdot z_{\mathrm{FW}} \\ -F_{\mathrm{C}} \cdot tanh\left(k \cdot (\dot{z}_{\mathrm{G}} - \dot{\theta}_{\mathrm{G}} \cdot b - \dot{z}_{\mathrm{FW}})\right) \cdot b = \left(F_{x_{\mathrm{RW}}} + F_{x_{\mathrm{FW}}}\right) \cdot h \\ \\ m_{\mathrm{FW}} \cdot \ddot{z}_{\mathrm{FW}} - c_{\mathrm{F}} \cdot \dot{z}_{\mathrm{G}} + c_{\mathrm{F}} \cdot b \cdot \dot{\theta}_{\mathrm{G}} + (c_{\mathrm{F}} + c_{\mathrm{T}}) \cdot \dot{z}_{\mathrm{FW}} - k_{\mathrm{F}} \cdot z_{\mathrm{G}} + k_{\mathrm{F}} \cdot b \cdot \theta_{\mathrm{G}} + (k_{\mathrm{F}} + k_{\mathrm{T}}) \cdot z_{\mathrm{FW}} \\ - F_{\mathrm{C}} \cdot tanh\left(k \cdot (\dot{z}_{\mathrm{G}} - \dot{\theta}_{\mathrm{G}} \cdot b - \dot{z}_{\mathrm{FW}})\right) = 0 \\ \\ I_{\mathrm{FW}} \cdot \ddot{\delta}_{\mathrm{FW}} = F_{x_{\mathrm{FW}}} \cdot R_{\mathrm{FW}} - M_{\mathrm{FB}} \\ \\ I_{\mathrm{RW}} \cdot \ddot{\delta}_{\mathrm{RW}} = F_{x_{\mathrm{RW}}} \cdot R_{\mathrm{RW}} + M_{\mathrm{RD}}, \end{cases} \tag{8}$$

ISSN: 2667-2812

 http://dx.doi.org/10.59490/65f89c8e269cb909bf53af3c

where $F_{x_{\mathrm{FW}}}$ and $F_{x_{\mathrm{RW}}}$ are the friction forces due to the tire–road interaction, and they are computed using the Pacejka Magic Formula (Pacejka, 2005), with constant coefficients as expressed in Equation (9). The formula uses dimensionless coefficients *B*, *C*, *D*, and *E*, which depend on the road condition, the slip factor κ, and the vertical load F_z acting on the considered wheel.

$$F_x = F_z \cdot D \cdot sin\Big(C \cdot arctan\Big(B \cdot \kappa - E \cdot \big(B \cdot \kappa - arctan(B \cdot \kappa)\big)\Big)\Big), \tag{9}$$

where M_{FB} is the brake torque acting on the front wheel. It is modeled as a Coulomb friction and is computed as in Equation (10):

$$M_{\mathrm{FB}} = 2 \cdot F_{\mathrm{BP}} \cdot R_{\mathrm{disc}} \cdot \mu_{\mathrm{disc}} \cdot tanh\big(k \cdot \dot{\delta}_{\mathrm{FW}}\big), \tag{10}$$

where F_{BP} is the force acting on the brake pad, R_{disc} is the effective brake disc radius, and μ_{disc} is the friction coefficient. A hyperbolic tangent function and a gain k are used to relate the friction torque to the sign of the relative front wheel velocity $\dot{\delta}_{\mathrm{FW}}$. The factor 2 stands for the number of friction interfaces on the brake.

3 Description and Characterization of the Validation Bicycle

In this section, the mobile test apparatus implemented on the e-bike and the specific measurements conducted to experimentally characterize its front suspension and tire are presented.

Figure 3 shows a Flyer Goroc 2, a crossover-type bike that will serve as a reference for the validation of the virtual model. It was instrumented with various sensors (see

ISSN: 2667-2812

 http://dx.doi.org/10.59490/65f89c8e269cb909bf53af3c

Table 2) to capture the in-plane dynamics of the bike during a strong braking maneuver with the front brake only.

Figure 3. Validation bicycle and equipment (different sensors used are circled)

The data logger, “AXX” (circled in dark green), recorded data from every channel and stored them on an external USB stick. It was mounted on the luggage rack and supplied by an external battery. The data acquisition system was also connected to a sensor switch, “AYY” (circled in red), which was able to collect data from four analog sensors and one frequency sensor. An inertial measurement unit (IMU) was directly included in the data logger; it measured accelerations and rotation rates in three directions. A force lever sensor, “A01” (circled in light green), was mounted on the front brake lever to measure the force applied by the rider when braking. The travel of the front suspension was logged using a linear potentiometer affixed parallel to the fork, “A02” (circled in purple).

ISSN: 2667-2812

 http://dx.doi.org/10.59490/65f89c8e269cb909bf53af3c

Table 2. Sensor characteristics

Measurand	Brake lever force	Fork displacement	Wheel speed	Acceleration/ rotation rate
Sensor name	2-D Debus Diebold SA-BS04-000	2-D Debus Diebold SA-LP150	2-D Debus Diebold SD-VI05-000	2-D Debus Diebold BC-3A4_3G500-000
Application	Brake lever	Fork	Front/rear wheels	Luggage rack
Principle	Strain gauge	Potentiometer	Inductive	Capacity effects/ Coriolis vibratory gyroscope
Range	0…500 N	0...150 mm	0...1,500 Hz	±4 g/±500 °/s
Accuracy	±0.5%	±1.5 mm	Depends on phonic wheel resolution	±1% /± 1%
Resolution	< 0.01 N	< 0.01 mm	Depends on data logger frequency	±0.00125 g/±0.02 °/s
Sampling rate	1 kHz	unlimited	< 50 kHz	1 kHz
Signaling	Voltage	Voltage	Voltage	CAN

The front wheel speed was recorded by an inductive sensor located near the front wheel axis, “A3X” (circled in yellow) and a phonic wheel with 60 ticks per revolution. It was used to measure the slip ratio of the front wheel during a braking maneuver. The rear wheel speed was measured in a similar way, “A03” (circled in blue), and only used as a bike speed reference. During the validation tests, only the front brake was used, so the slip ratio of the rear wheel could be neglected. Furthermore, the amount of braking force was kept in a range where no lift of the rear wheel could occur. All signals were logged with a sample frequency of 1 kHz.

While the force on the front brake pad could not be measured on the bike during tests, it was possible to experimentally determine the amplification factor between the force applied on the lever and the effective force on the brake caliper. For this reason, the brake system was removed from the bike, and an additional force sensor was mounted between the brake pads. This force sensor was a CLP/14kN used in conjunction with a CMD600 amplifier (both from HBM). Force steps were applied on the brake lever and the information delivered by both sensors was recorded. The measured points with the most significant population (steady state points) were averaged, while the points with the least significant population (transient points) were not considered. Finally, a function that went through the averaged points and interpolated linearly between them was designed (see Figure 4). With this function, it was possible to transform the force measured at the brake lever during the validation tests into a force at the front brake pad that served as an input to the virtual bike model. Interestingly, the interpolation function still provided good accuracy during transients.

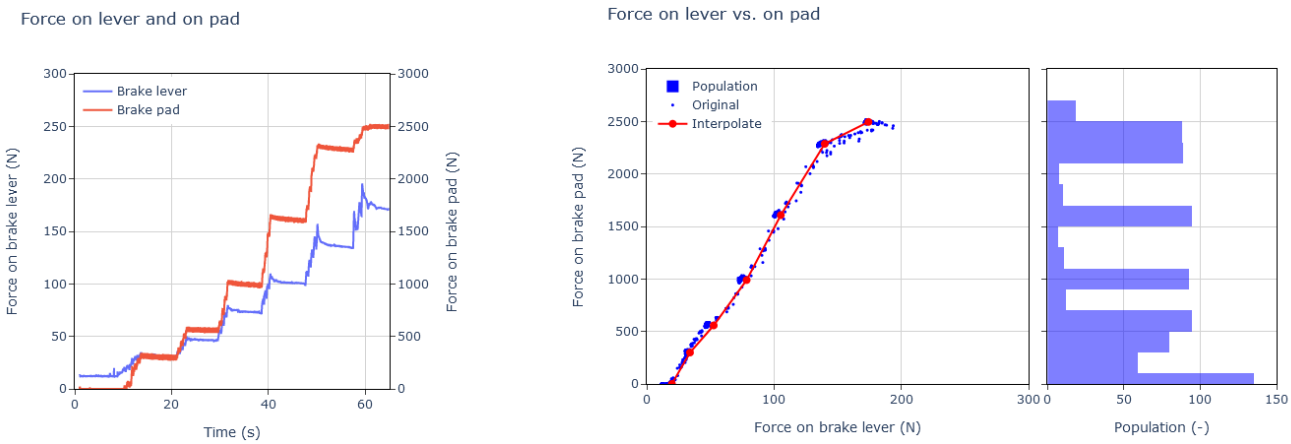

Figure 4. Interpolation function used to transform the force measured on the brake lever into a force at the brake pad: the measurements (left panel) and the correlation between measurements and the interpolation function (right panel)

ISSN: 2667-2812

 http://dx.doi.org/10.59490/65f89c8e269cb909bf53af3c

For the experimental characterization of the front suspension, SR Suntour Raidon 34–120 mm, and the front tire, Maxxis Forekaster SilkShield 29 × 2.35, a servo-hydraulic double-rod test cylinder was used. It could test components statically with a force of ±25 kN and dynamically with a force of ±20 kN; the maximum displacement allowed was 150 mm (±75 mm) at a maximum speed of 1.8 m/s and a maximum frequency of 100 Hz. It was used to apply a displacement cycle as an input to the upper part of the fork.

Figure 5 shows the test setups used to identify the behavior of the front suspension and the tire. The rod of the hydraulic cylinder was equipped with a force sensor and a displacement sensor directly connected to the steerer tube. In the first test setup, a sinusoidal displacement was applied to the suspension alone, and the reaction force was measured for different amplitudes and frequencies. These measurements were used to identify suspension stiffness, damping, and Coulomb friction. In the second setup, the suspension was measured together with the front wheel and tire to determine the compression stiffness and damping of the tire at different inflation pressures. In this latter setup, a mount supported the wheel axis vertically (direction normal to the picture plane) to prevent any bending of the assembly under the test load.

Figure 5. Experimental setups on a dynamical test bench to characterize suspension and tire behavior: the setup with fork suspension alone (left panel) and the setup with both fork and front tire (right panel)

Based on the suspension measurements, constant friction, stiffness, and damping parameters—namely k_{F}, c_{F}, F_{CF}, k_{T}, c_{T}—could be estimated, and a good agreement was found for suspension travels up to a compression of approximately 70 mm and relative velocities up to 125 mm/s (see Figure 6, left panel). For further compression, the constant-parameter model did not reproduce the increasing stiffness of the suspension (see Figure 6, right panel). Although the maximum travel of the tested suspension model was approximately 120 mm, no measurements were available beyond a compression of 90 mm.

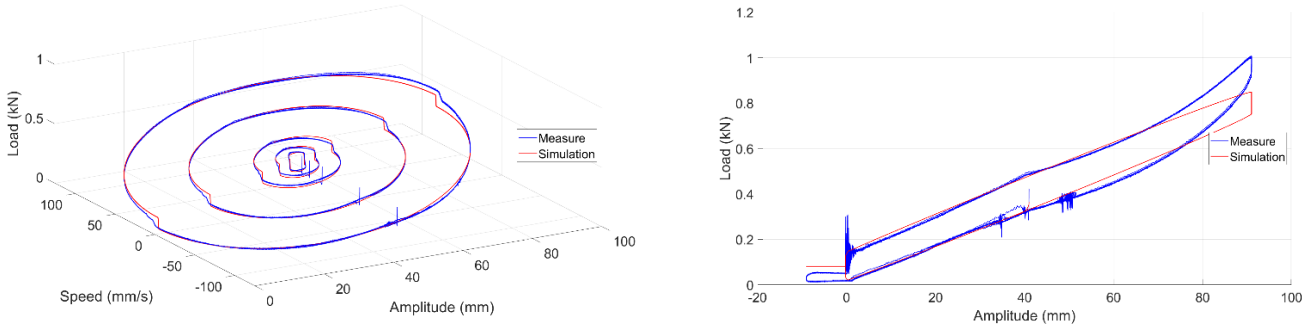

Figure 6. Validation of the suspension model in response to a sinusoidal displacement of different amplitudes displayed here at a frequency of 0.5 Hz with 0 mm corresponding to uncompressed suspension: amplitudes of ±2 mm, ±5 mm, ±10 mm, ±25 mm, ±40 mm (left panel); amplitude of ±50 mm showing increasing stiffness for a suspension travel beyond 70 mm (right panel)

ISSN: 2667-2812

 http://dx.doi.org/10.59490/65f89c8e269cb909bf53af3c

4 Validation of the Simulation Model

In this section, the fidelity of the simulation model is assessed by comparing its results with measurements. The test scenario consisted of accelerating the e-bike on a flat road until reaching a speed of approximately 25 km/h, stabilizing the bike by ceasing pedaling for about 1 second, and braking strongly with the front brake until the bike came to a complete stop. Although the rider tried to remain immobile with respect to the bicycle frame during the braking phase, this was essentially impossible in the very late phase of braking. The tests were performed only on a clean, dry, high-grip surface so that any locking of the front wheel was made impossible and braking intensity was kept in a range where no lift of the rear wheel could occur.

The simulation model had only one input variable, namely the normal force applied at the front brake caliper, which was obtained from the measured force at the brake lever as detailed in Section 3. Numerical values of the parameters used for the presented simulation results are available in Ramosaj's (2023) GitLab repository. Mass distribution and inertias for the combined bike and rider were approximated from Moore's (2009) and Maier's (2018) data, while the Pacejka coefficients were identified from the friction measurements conducted on Schwalbe tour tires as presented in Klug's (2017) study.

Figure 7 compares the simulation results and the physical measurements of the bicycle based on the scenario described above. The agreement between the simulation and measurements was good for front wheel speed and longitudinal acceleration, the two most important quantities since they are the two inputs of the ABS. The overall deceleration of the front wheel speed was well reproduced by the model. However, the relatively high wheel slip measured at the start of braking was only partially visible in the simulation results. This may have been due to the use of a steady-state version of the magic formula for tire modeling, which is unable to account for transient effects. The measurement of longitudinal acceleration was rather noisy, mainly due to the irregularities of the road, which was not totally smooth, and the driver, whose movement was not totally negligible. However, the simulated acceleration corresponded well to the average of the measured signal, which validates the model. Interestingly, to compare the simulated longitudinal acceleration with the measured acceleration, it was necessary to take into account the terrestrial gravity component that appeared on the IMU measurement axis when the bike underwent a pitch angle, as this component could be significant even at small pitch angles.

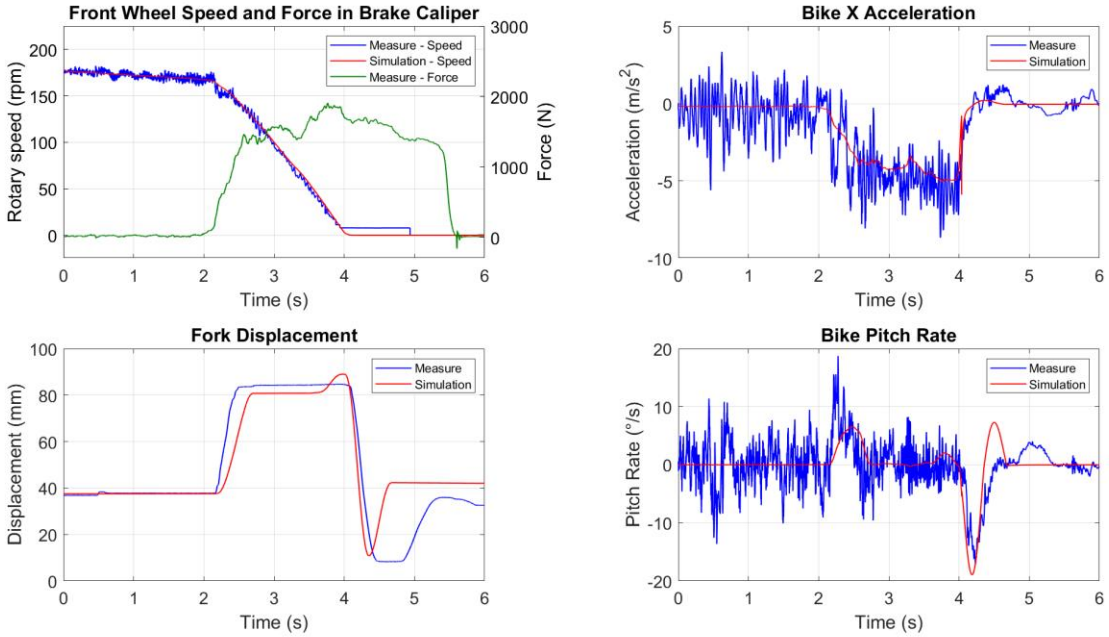

Figure 7. Comparison of the simulation model (red) and the physical bike (blue) when submitted to the same brake force input

A comparison of fork displacement and pitch velocity highlights certain weaknesses in the approach taken to suspension modeling. First, as shown in Figure 6, the actual suspension stiffness was not well captured by our constant-stiffness model, which resulted in a deviation between measured and simulated fork travel, especially for large compression values. Second, while the extension of the suspension model at the end of the braking phase occurred with a slightly too steeply decreasing slope, its compression at the

ISSN: 2667-2812

 http://dx.doi.org/10.59490/65f89c8e269cb909bf53af3c

beginning of the braking phase was slower than in the measurements. In other words, the observed peak in pitch velocity during pitch-up was slightly overestimated, while the peak during nose dive was clearly underestimated compared to the measurement. One explanation is that the suspension may have had different damping in compression and extension, particularly at high relative speeds, which was not taken into account in the proposed suspension model.

5 Hardware-in-the-Loop Test Bench

In this section, the developed HiL test bench is presented, and its applicability to an ABS validation process is discussed. Figure 8 presents an overview of the installation, whose core part is the real-time target machine running the virtual bike model connected to the physical braking system of the bike.

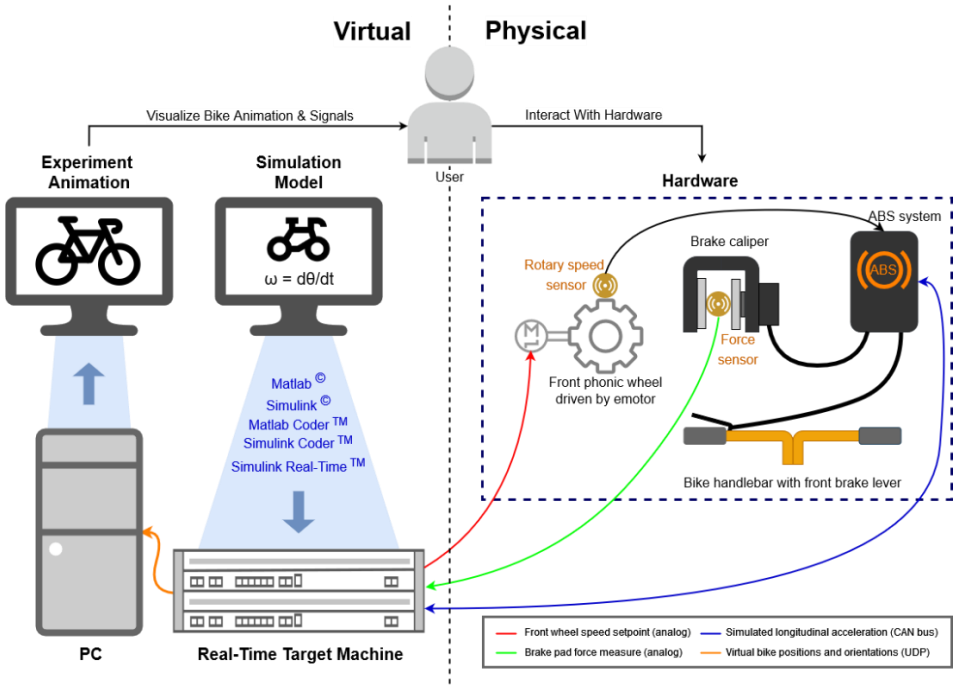

Figure 8. A complete overview of the hardware-in-the-loop test bench

The HiL test bench featured ergonomically positioned bicycle handlebars for use in real-life situations. The front brake lever was hydraulically connected to the ABS hydraulic module, which was, in turn, connected to the brake caliper. A force sensor (CLP/14kN from HBM) was placed between the brake pads and adjusted to the same thickness as a brake disc. The measured force was the input variable for the virtual bike model. A phonic wheel was driven by a fast-reacting DC motor whose speed set point was defined by the real-time simulation model. This emulated the rotation of the bike's front wheel so that the ABS speed sensor could be used to acquire the rotation speed signal as in the real world. The ABS under test also needed the bicycle's longitudinal acceleration as an input signal. In real-life operation, this acceleration is received from an on-board IMU, but in the HiL configuration, this acceleration was calculated by the simulation model and sent to the ABS control unit via a CAN bus.

Figure 9 illustrates the current installation of the HiL test bench. A pneumatic cylinder acts on the brake lever and can apply a force of up to 200 N. This makes it possible to run scenarios with different sets of parameters with good reproducibility. The entire HiL test bench was clocked at a frequency of 1 kHz. Simulink's fixed-step Extrapolation solver (ODE14x) was used to numerically integrate the ordinary differential equations of the virtual bicycle model. The integration time step must be chosen carefully to ensure correct convergence, even in the case of strong discontinuities in the inputs (e.g., sudden braking) or in the intrinsic behavior of the system (e.g., wheel locking). Although it is possible to reduce the time step to 0.2 ms without overloading the target machine's CPU in real time, a time step of 1 ms is sufficient in most cases.

ISSN: 2667-2812

 http://dx.doi.org/10.59490/65f89c8e269cb909bf53af3c

Figure 9. Developed HIL test bench: overview (left panel); handlebar, brake system, and ABS (right panel)

Figure 10 shows the typical results obtained for the following scenario: a large force is suddenly applied and held constant by the test bench's pneumatic cylinder. This force corresponds to a constant force of 1,000 N on the front brake pads without ABS intervention. The scenario tested considered a flat road with a low grip so that the braking torque applied exceeded the maximum friction force the tire could transmit to the road. When an excessive slip of the wheel was detected, the ABS triggered a pressure release in the hydraulic brake circuit, reducing the actual force measured at the front brake pad. When the slip of the front wheel was reduced, the pressure in the hydraulic brake circuit increased again, at first slowly and then with a steeper slope. The results show that, with the ABS, the wheel does not lock for a significant period of time. However, it reaches a speed close to zero for a short time, suggesting that ABS performance can be improved in these specific test conditions.

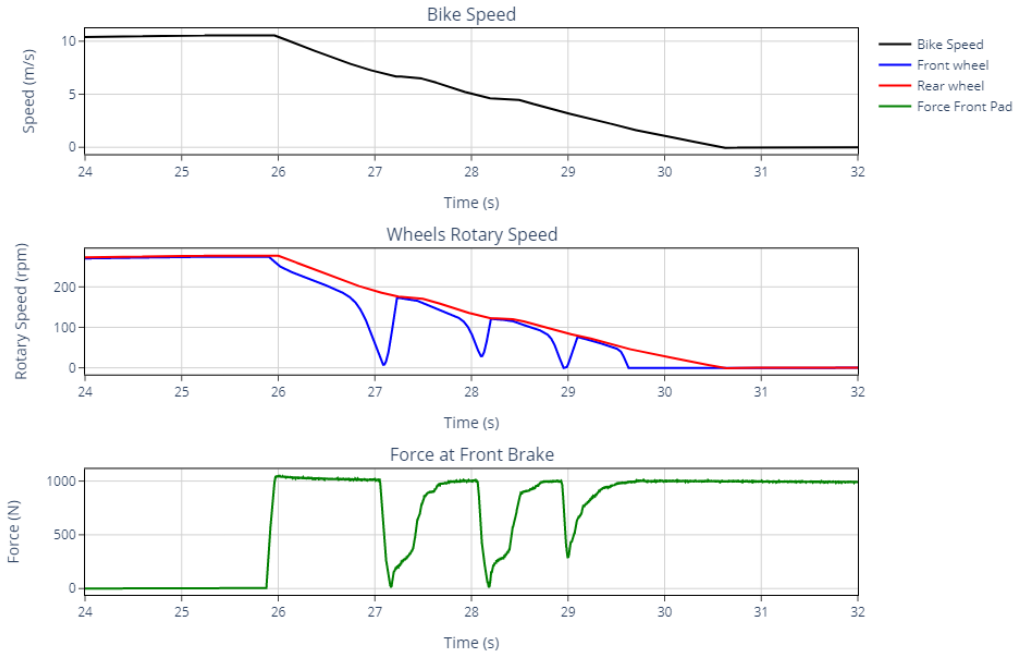

Figure 10. Example results obtained with the HiL test bench (the test scenario shows that ABS triggers a decrease of effective force at the front brake when an excessive slip condition is detected at the front wheel)

The HiL test bench presented here is based on a virtual bike model that has been validated for a specific load case but that is fully parameterizable, making it easy to simulate these different load cases by varying, for example, the position of the CoG, the rider's mass, or tire characteristics. In the current situation, the test bench is operational and can already provide useful information, for example, to an e-bike manufacturer wishing to validate the performance and robustness of an ABS on its bicycle.

ISSN: 2667-2812

However, the discrepancies presented in Section 5 between the behavior of the virtual bike and the measurements should prompt one to draw cautious conclusions. In particular, as the wheel speed and longitudinal acceleration obtained from the virtual bike simulation model were relatively smooth, they did not allow us to test the ability of the ABS control logic to process the much noisier signals that would be acquired during real-life operation on the road.

One of the limitations of the test bench is the need to provide the ABS hardware under test with suitably conditioned inputs. In the case where the only input required by the ABS is the measurement of wheel speed, it is relatively simple to emulate the rotation of a phonic wheel and thus place the ABS sensor in operating conditions as close to reality as possible. However, if the ABS control logic requires acceleration information, it is not possible to have a device on the test bench that emulates this acceleration. This involves bypassing the IMU and sending the ABS control unit a signal representing the accelerations based on the simulation model. Ultimately, the disadvantage of this approach is that it makes interfacing between the virtual and physical worlds more complex, and it requires the cooperation of the ABS manufacturer to enable the control unit to receive an external signal.

6 Conclusions and Outlook

This paper presented the development of an HiL test bench that can be used to test the correct operation of an ABS on an e-bike. The HiL setup was based on a virtual bike model with six degrees of freedom, which was validated by on-road measurements on an instrumented bike and additional dynamic testing of the front suspension. Tests carried out as part of this development show that the developed test bench can be interfaced with an existing ABS and that it can easily be used to test different scenarios, such as emergency braking on a flat road with low grip, and different load cases, such as a child seat or panniers. The HiL test bench can be used by ABS manufacturers to improve their development processes using model-based design techniques or by e-bike manufacturers to validate the performance of a supplier's ABS in a quantitative, safe, and reproducible way. The simulation model proposed in this paper is adequate and sufficient, since it reproduces with good correlation the front wheel speed profile and the longitudinal acceleration profile, which are typically the two input quantities of an ABS. However, there is still room for improvement in reducing the discrepancies observed between measurements and simulation during strong braking. In particular, the nonlinear behavior of the suspension needs to be modeled in greater detail, and more complex tire models that can account for transient effects should be investigated.

7 References

Corno, M., D'Avico, L., & Savaresi, S. M. (2018). An anti-lock braking system for bicycles. *In 2018 IEEE Conference on Control Technology and Applications*, 834–839.

Cossalter, V. (2006). *Motorcycle dynamics*. LuLu.

Enisz, K., Szalay, I., Fodor, D., Nagy, K., & Jakab, R. (2012). Bicycle anti-lock braking system prototype development. *Acta Universitatis Sapientiae Electrical Mechanical Engineering, 4*, 45–57.

Gomez, M. (2001). Hardware-in-the-Loop Simulation. *Embedded Systems Design*, *14*(13), 38–49.

Haufe, S., Boeck, H. T., Häckl, S., Boyen, J., Kück, M., van Rhee, C. C., Graf von der Schulenburg, J.-M., Zeidler, J., Schmidt, T., Johannsen, H., Holzwart, D., Koch, A., & Tegtbur, U. (2022). Impact of electrically assisted bicycles on physical activity and traffic accident risk: a prospective observational study. *BMJ Open Sport & Exercise Medicine, 8(4)*, e001275.

Klug, S., Moia, A., Verhagen, A., Görges, D., & Savaresi, S. M. (2017). Effectiveness of actuating on rectilinear bicycle braking dynamics. *IFAC-PapersOnLine*, *50*(1), 972–979.

Maier, O., Pfeiffer, M., & Wrede, J. (2015). Development of a braking dynamics assistance system for electric bicycles: Design, implementation, and evaluation of road tests. *IEEE/ASME Transactions on Mechatronics*, *21*(3), 1671–1679.

Maier, O. (2018). *Modellbasierte Entwicklung eines aktiven Sicherheitssystems für elektrifizierte Fahrräder* [PhD thesis, Otto-von-Guericke-Universität Magdeburg].

Moore, J. K., Hubbard, M., Kooijman, J. D. G., & Schwab, A. L. (2009, January). A method for estimating physical properties of a combined bicycle and rider. In *International Design Engineering Technical Conferences and Computers and Information in Engineering Conference*: *Vol. 49019. Vehicle Systems and Tire Dynamics* (pp. 2011–2020). ASME. https://doi.org/10.1115/DETC2009-86947

Pacejka, H. (2005). *Tire and vehicle dynamics*. Elsevier.

Pfeiffer, M., Wrede, J., Steeb, S. (2020). Validation of a bicycle dynamics assistance system using hardware-in-the-loop simulation. *Proceedings of Bicycle and Motorcycle Dynamics 2019, Symposium on the Dynamics and Control of Single Track Vehicles, Italy*. https://doi.org/10.6084/m9.figshare.12363701.v1

Ramosaj, N. (2023). *BMD2023-ramosaj-fusco-viennet*. GitLab repository. https://gitlab.forge.hefr.ch/nicolas.ramosaj/bmd2023-ramosaj-fusco-viennet

VDI 2206. (2004). Design methodology for mechatronic systems. VDI 2206:2004–06.

ISSN: 2667-2812